Translational Science

Cancer Research

Fc-Mediated Anomalous Biodistribution of Therapeutic Antibodies in Immunodeficient Mouse Models

Sai Kiran Sharma[1], Andrew Chow[2], Sebastien Monette[3], Delphine Vivier[4], Jacob Pourat[1], Kimberly J. Edwards[1], Thomas R. Dilling[1], Dalya Abdel-Atti[1], Brian M. Zeglis[1,4], John T. Poirier[2], and Jason S. Lewis[1,5,6]

Abstract

A critical benchmark in the development of antibody-based therapeutics is demonstration of efficacy in preclinical mouse models of human disease, many of which rely on immunodeficient mice. However, relatively little is known about how the biology of various immunodeficient strains impacts the *in vivo* fate of these drugs. Here we used immunoPET radiotracers prepared from humanized, chimeric, and murine mAbs against four therapeutic oncologic targets to interrogate their biodistribution in four different strains of immunodeficient mice bearing lung, prostate, and ovarian cancer xenografts. The immunodeficiency status of the mouse host as well as both the biological origin and glycosylation of the antibody contributed significantly to the anomalous biodistribution of therapeutic monoclonal antibodies in an Fc receptor-dependent manner. These findings may have important implications for the preclinical evaluation of Fc-containing therapeutics and highlight a clear need for biodistribution studies in the early stages of antibody drug development.

Significance: Fc/FcγR-mediated immunobiology of the experimental host is a key determinant to preclinical *in vivo* tumor targeting and efficacy of therapeutic antibodies. *Cancer Res; 78(7); 1820–32. ©2018 AACR.*

Introduction

Antibodies have evolved from being ancillary biochemical reagents in laboratory research to taking center stage as powerful drugs that are used in the clinic to treat cancer and immune-mediated disorders (1, 2). By the end of 2014, the list of 47 antibody therapeutics approved and marketed in the United States and EU was growing at an average approval rate of 4 new products per year (3). Despite the high failure rate (~86%) in the drug development process of antibody-based therapeutics, growth projections predicted that there would be approximately 70 new mAb-based drugs on the market by 2020 (3, 4). Since 2015, 25 new antibody products have received first approvals in the United States alone and 7 antibodies are under review by the FDA (http://www.antibodysociety.org/news/approved-antibodies/).

Much of this progress has been made hand-in-glove with a co-evolution in the role of mice in preclinical research. Initially used as naïve hosts for the production of murine mAbs, today transgenic mice are capable of generating fully human antibodies (5–9). Mice provide an excellent preclinical platform to model a wide spectrum of human diseases and investigate diagnostic and therapeutic strategies (10–13). Together, these advances have birthed a thriving billion-dollar biopharmaceutical industry and are transforming biomedical research and clinical practice (3, 14).

More recently, increased activity in the preclinical development and testing of antibody–drug conjugates (ADC) and therapeutic antibody-based formulations have provided an impetus for the integration of molecular imaging in drug development programs (15, 16). The inclusion of noninvasive imaging of disease biomarkers in the design of clinical trials for antibody-based therapeutics can impact clinical outcomes by virtue of the ability of imaging to (i) identify patients who may be eligible for treatment with targeted therapies, (ii) inform the dosing of patients based on the *in vivo* expression levels of the biomarker, and (iii) evaluate response to treatment (17–19). There has been a surge of reports demonstrating the successful translation of immunoPET tracers in the cancer clinic (20–22). ImmunoPET allows the noninvasive evaluation of disease burden *in vivo* and facilitates the creation of a companion diagnostic agent to a therapeutic antibody. Furthermore, an immunoPET tracer provides a window of opportunity to visualize the prospective *in vivo* pharmacokinetics and biodistribution of its therapeutic counterpart.

Despite the critical importance of these studies, experimental parameters such as the biology of the preclinical host (the

[1]Departments of Radiology and the Molecular Pharmacology Program, Memorial Sloan Kettering Cancer Center, New York, New York. [2]Department of Medicine, Memorial Sloan Kettering Cancer Center, New York, New York. [3]Laboratory of Comparative Pathology, Memorial Sloan Kettering Cancer Center, Weill Cornell Medicine, and The Rockefeller University, New York. [4]Department of Chemistry, Hunter College and the Ph.D. Program in Chemistry, the Graduate Center of the City University of New York, New York, New York. [5]Departments of Radiology and Pharmacology, Weill Cornell Medical College, New York, New York. [6]Radiochemistry and Molecular Imaging Probes Core, Memorial Sloan Kettering Cancer Center, New York, New York.

Note: Supplementary data for this article are available at Cancer Research Online (http://cancerres.aacrjournals.org/).

Corresponding Authors: Jason S. Lewis, Department of Radiology, Memorial Sloan Kettering Cancer Center, 1275 York Avenue, NY 10065. Phone: 646-888-3038; Fax: 646-888-3059; E-mail: lewisj2@mskcc.org; and John T. Poirier, poirierj@mskcc.org

doi: 10.1158/0008-5472.CAN-17-1958

mouse strain), the biological origin and glycosylation status of the antibody and its interaction with other components of the immune system that might affect the *in vivo* performance of a therapeutic antibody are frequently overlooked. In this report, we comprehensively evaluate the biodistribution of humanized, chimeric, and murine mAbs via immunoPET imaging in four immunodeficient mouse strains and investigate the impact of the endogenous levels of immunoglobulins in the preclinical host as well as the glycosylation status of the antibody on its *in vivo* pharmacologic profile.

Materials and Methods

Cell culture and xenografts

All cell lines used in this study were obtained from the ATCC in 2009 and used between passages 3–9 after thawing to ensure complete revival. In addition to routine testing for the presence of mycoplasma, the identity and purity of the cells was validated via short tandem repeat profiling. The cells were cultured in ATCC-recommended media under aseptic conditions in an incubator providing humidified atmosphere of 5% CO_2 in air (see Supplementary Data for details). All protocols described for animal experiments were approved by the Institutional Animal Care and Use Committee at Memorial Sloan Kettering Cancer Center (New York, NY). Four strains of immunodeficient mice –Nu/Nu (Crl:NU-*Foxn1*^{nu}; Strain Code: 088; Charles River Laboratories), SCID/NCr (CB17/lcr-*Prkdc*^{scid}/lcrCr; Strain Code: 561; Charles River Laboratories), NOD SCID (NOD.CB17-*Prkdc*^{scid}/NcrCrl; Strain Code: 394; Charles River Laboratories), and NOD SCID gamma (NOD.Cg-*Prkdc*^{scid}*IL2rg*^{tm1Wjl}/SzJ; Stock No: 005557; The Jackson Laboratory), referred to as NSG mice, were used to generate subcutaneous xenograft models (see Supplementary Data for details).

Radioimmunoconjugate synthesis

A DLL3-targeted humanized mAb hSC16 and an Fc-silent variant (*Fc-N297A* mutant) of hSC16 having near-identical binding affinities for DLL3 (~2.4 nmol/L; Supplementary Fig. S1A and S1B; Supplementary Table S1), and a murine mAb targeting DLL3 with a binding affinity of ~0.5 nmol/L (Supplementary Fig. S1C and Supplementary Table S1) were obtained from Abbvie Stemcentrx LLC. Other therapeutic antibodies including a HER2-targeted humanized IgG1 trastuzumab, a PSMA-targeted humanized IgG1, huJ591, an EGFR-targeted chimeric antibody, cetuximab were obtained from the pharmacy at Memorial Sloan Kettering Cancer Center and modified to generate immunoconjugates that were radiolabeled with zirconium-89 (^{89}Zr; $t_{1/2}$ = 78.4 hours). The post-radiolabeling immunoreactivity of hSC16 to bind with DLL3-expressing H82 cells was tested in radioligand binding assays (Supplementary Fig. S2). Bioconjugation and radiolabeling of the mAbs used in this study yielded radioimmunoconjugates in >99% radiochemical purity and molar specific activities of 31.95–39.24 GBq/μmol; (5.7–7.0 mCi/mg). To avoid inter-batch variability in the radiosynthesis and testing of a given radiolabeled antibody construct, all the steps starting from radioimmunoconjugate synthesis to the final injection of the antibody-based tracer in multiple immunodeficient strains of xenograft mice were performed contemporaneously as a single experiment.

In vitro characterization of deglycosylated and Fc-silent hSC16 immunoconjugates

A glycoengineered variant of the hSC16 immunoconjugate was prepared via enzymatic deglycosylation using 1 unit of PNGaseF (New England Biolabs) per microgram of DFO-conjugated hSC16 antibody (DFO-hSC16). Five micrograms of the following antibody constructs—an isotype-matched humanized antibody (hIgG; 23, 24; provided by Abbvie Stemcentrx LLC), hSC16, DFO-hSC16, deglycosylated DFO-hSC16, and DFO-conjugated Fc-silent variant of hSC16 (DFO-hSC16_Fc-silent)—were electrophoresed on a NuPAGE 4%–12% Bis-Tris gel (Thermo Fisher Scientific). The gel was stained with Coomassie blue to observe a shift in the migration of heavy chains in the deglycosylated and Fc-silent hSC16 immunoconjugates. A Western blot analysis was performed and the nitrocellulose membrane was stained with Ponceau-S to confirm the successful transfer of antibody heavy chains from the gel. Finally, a carbohydrate analysis was performed using lens culinaris agglutinin (LCA; Vector Laboratories) to establish the presence versus absence of glycans in the various antibody constructs (see Supplementary Data for details).

PET imaging

PET imaging experiments were conducted on an Inveon PET/CT scanner (Siemens). Xenograft mice (n = 2 per strain) were injected with the relevant immunoPET tracer [7.4 – 9.25 MBq; (200 – 250 μCi), 35–44 μg in chelex-treated PBS] via the lateral tail vein. Owing to the slow *in vivo* pharmacokinetics of full-length antibodies, static PET scans were acquired between 140 and 148 hours (day 6) after the injection of the radiotracer. At this time, the vast majority of the antibody-based radiotracer would have cleared from systemic circulation while concomitantly achieving accretion in the respective target antigen-expressing tumors. PET images were analyzed using ASIPro VM software (Concorde Microsystems).

Biodistribution

Xenograft mice (n = 3–4 per group) were injected with the relevant tumor-targeting radioimmunoconjugate [0.925–1.11 MBq (25–30 μCi), 4.4–5.2 μg in 200 μL chelex-treated PBS] via the lateral tail vein. To saturate Fc-mediated uptake, an additional cohort of Nu/Nu, NOD SCID, and NSG xenograft mice were administered the aforementioned dose of the relavant radiotracer mixed with 220 μg (50-fold excess by mass) of unlabeled isotype-matched humanized antibody. The animals were euthanized by CO_2(g) asphyxiation between 140 and 148 hours after the injection of the radioimmunoconjugates. Upon euthanasia, relevant tissues (including tumor) were removed, rinsed in water, dried in air for 5 minutes, weighed, and counted in a gamma counter calibrated for ^{89}Zr. Counts were converted into activity using a calibration curve generated from known standards. Count data were background- and decay-corrected to the time of injection, and the percentage of injected dose per gram (%ID/g) for each tissue sample was calculated by normalization to the total activity injected.

Generation of splenectomized H82 xenografts in NSG mice

Ten 6- to 8-week-old NSG mice were splenectomized (see Supplementary Data for details). Ten days later, 3 million DLL3-positive H82 cells were subcutaneously implanted in the

right flank of each mouse and allowed to grow for 2 weeks before using the animals for PET imaging and biodistribution studies.

Ex vivo analysis

Histopathologic evaluation of the mice was performed via partial necropsies to isolate organs that had high activity concentrations in biodistribution studies. To identify any additional manifestation of toxicity, complete necropsies with histopathologic examination of all major organs was performed in two NSG mice that were injected with an imaging dose (~250 μCi; 9.25 MBq) of ^{89}Zr-labeled hSC16. Tissues were harvested and fixed in 10% neutral buffered formalin, routinely processed in alcohol and xylene, embedded in paraffin, sectioned at 5-μm thickness, and stained with hematoxylin and eosin (H&E). IHC staining with myeloperoxidase was performed to identify myeloid cells in sections of the spleen and bone marrow obtained from Nu/Nu and NSG mice. The slides were evaluated by a board certified veterinary pathologist, (S. Monette; see Supplementary Data for more details).

Immunoglobulin titers were evaluated in the sera obtained from 6- to 10-week-old experimentally naïve female mice ($n = 3$–5) of all four immunodeficient mouse strains using commercially available mouse Ig ELISA kits (Thermo Fisher Scientific). The level of expression of various Fc-gamma receptors (FcR) in Nu/Nu versus NSG mice was analyzed in *ex vivo* flow cytometry experiments. To this end, the spleen, liver, and bone marrow from mice were harvested and processed to isolate immune cells, which were stained for analysis via flow cytometry. The goal of this exercise was to compare the cellular composition and abundance of FcR expression on myeloid cell populations in Nu/Nu versus NSG mice. To further identify the *in vivo* immune cell destination of hSC16 in Nu/Nu versus NSG mice, the antibody was labeled with fluorescein isothiocyanate (FITC) using an amine-reactive antibody labeling kit (Thermo Fisher Scientific) to create hSC16-FITC. The latter was injected in five 6- to 8-week-old nontumor bearing female Nu/Nu versus NSG mice 144 hours prior to using the animals for *ex vivo* flow cytometry experiments. One mouse of each strain was not injected with hSC16-FITC, so it could serve as a fluorescent minus one (FMO) control. The results obtained from flow cytometry experiments were processed using FlowJo software and analyzed for statistical significance using GraphPad Prism 7 (see Supplementary Data for details).

Statistical analysis

All biodistribution data are expressed as means ± SD. Where applicable, statistical differences were analyzed by unpaired two-tailed *t*-test using GraphPad Prism 7 software. Comparisons with P values <0.05 were considered significant.

Results

Comparative *in vivo* imaging and biodistribution of mAbs

We investigated the *in vivo* fate of therapeutic mAbs targeting four distinct cell surface therapeutic targets—DLL3, PSMA, HER2, and EGFR in mouse xenograft models of small-cell lung cancer, prostate cancer, ovarian cancer, and squamous cell carcinoma, respectively. ImmunoPET with DLL3-targeted ^{89}Zr-labeled hSC16 delineated subcutaneously xenografted H82 small-cell lung cancer tumors in all immunodeficient strains. Notably, the highest contrast images were seen in Nu/Nu mice. In contrast, all other more immunodeficient strains, SCID, NOD SCID, and NSG, yielded lower PET avidity in H82 tumors and relatively higher activity concentrations in nontarget organs such as the appendicular skeleton, the pelvic girdle, the spleen, and the liver (Fig. 1A–D).

Ex vivo biodistribution studies in the various strains of mice corroborated the results from PET imaging. Nu/Nu mice xenografts yielded maximum concentration of activity in the H82 tumors (24.9% ± 4.4% ID/g), with ≤6% ID/g in nontarget organs (Supplementary Table S2). H82 xenografts in the more immunodeficient strains of mice, NOD SCID and NSG, showed poor tumor uptake and displayed an inverse correlation between the concentration of activity in the tumors (~ 4% ID/g) versus nontarget organs such as the spleen (≥ 60% ID/g) and bones (≥13% ID/g; Supplementary Table S2). These studies revealed an association between the anomalous off-target *in vivo* biodistribution and the degree of immunodeficiency of the preclinical host.

Fc Receptor involvement and modulation of nonspecific uptake

Mouse spleen and bones lack expression of DLL3. We therefore hypothesized that the exceptionally high radioactivity concentration in these tissues may be mediated by the interaction of the Fc-portion of hSC16 with one or more FcRs expressed by myeloid cells *in vivo* (23, 24). To test this hypothesis, Nu/Nu, NOD SCID, and NSG mice bearing H82 xenografts were administered 4.4–5.2 μg of ^{89}Zr-labeled hSC16 coinjected with 220 μg of an isotype-matched humanized antibody to occupy and engage the FcRs *in vivo*. PET imaging of H82 xenografts in NSG mice that were injected with approximately 25-fold excess (~1 mg) of unlabeled isotype IgG control 20 minutes prior to an imaging dose of ^{89}Zr-labeled hSC16, revealed a high uptake of the radiotracer in the H82 tumor and low uptake in the bones, liver, and spleen (Fig. 1E). *Ex vivo* biodistribution studies carried out 144 hours after the coinjection of ^{89}Zr-labeled hSC16 and the unlabeled isotype control antibody revealed almost no impact on the pattern of radioactivity concentration in Nu/Nu mice xenografts, but a dramatic change in the biodistribution pattern of the antibody tracer in the highly immunodeficient mice strains: NOD SCID and NSG (Fig. 1F). A remarkable (~10-fold) increase in tumor uptake was observed in both these strains of mice, with a concomitant 8- to 10-fold drop in the concentration of activity in the spleen. Although less dramatic, a 2-fold decrease in the activity concentrations was observed in the liver and bone tissues (Supplementary Table S2).

The glycosylation of the Fc portion of immunoglobulins plays a critical role in their interaction with FcRs (25). We chemoenzymatically deglycosylated hSC16 to abrogate the interaction between the Fc portion of ^{89}Zr-labeled hSC16 and Fc receptors (FcR) expressed on myeloid cells *in vivo*. In addition, an Fc-silent variant of the hSC16 was used to further validate the role of Fc–FcR interaction leading to the anomalous biodistribution observed in the highly immunodeficient NOD SCID and NSG xenograft mice. Efficient deglycosylation of DFO-hSC16 and the putative absence of glycans in the DFO-hSC16 Fc-silent immunoconjugate were apparent from a similar downward shift in the migration of the heavy chains upon gel electrophoresis of these constructs (Fig. 2A). A successful transfer of the antibody heavy chains from the gel to the nitrocellulose membrane was evidenced via Ponceau S staining (Fig. 2B). Finally, the biotinylated LCA blot (Fig. 2C) unequivocally established the absence of

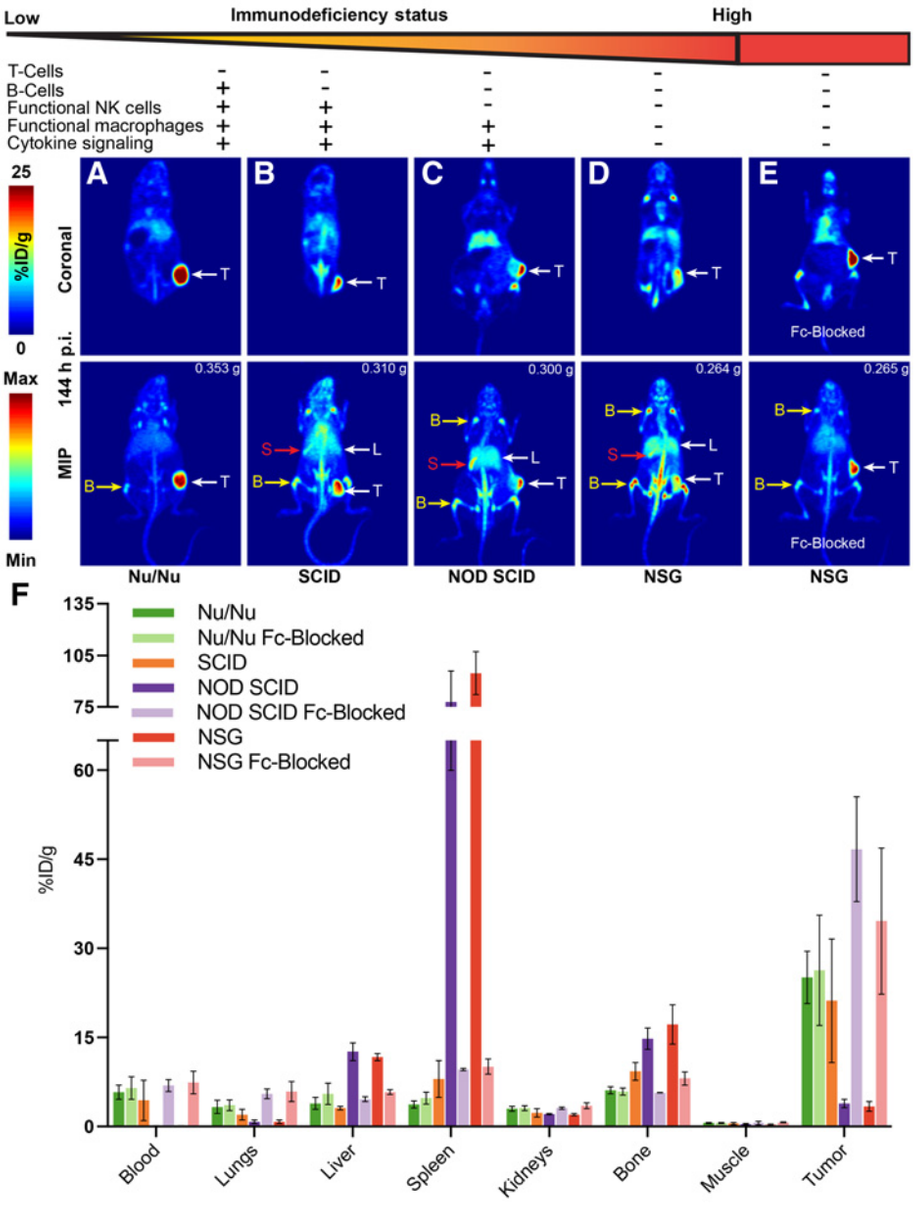

Figure 1.

Degree of immunodeficiency of the preclinical host is associated with increased anomalous biodistribution and inefficient *in vivo* tumor targeting of humanized therapeutic antibodies. **A–D,** Coronal slices and maximum intensity projection PET images (MIPs, 0%–100%) acquired between 140 and 148 hours after the injection of ^{89}Zr-labeled hSC16 in subcutaneous H82 xenografts developed in mice with different degrees of immunodeficiency (increasing from left to right): Nu/Nu < SCID << NOD SCID <<< NSG. Arrows indicate the tumor (T), spleen (S), bone (B), and liver (L). **E,** Restoration of ^{89}Zr-labeled hSC16-associated activity concentration in H82 tumor and a concomitant decrease in activity in nontarget organs by preinjection of a 25-fold excess of a humanized isotype control. **F,** *Ex vivo* biodistribution analysis of ^{89}Zr-labeled hSC16 at 144 hours after the injection of the tracer with and without 25-fold excess of humanized isotype control that serves as an Fc-block in xenograft mice with high immunodeficiency status ($n = 4$ mice per group). Tumor weights are mentioned at the top right hand corner of the MIP images. %ID/g values are shown in Supplementary Table S2.

the carbohydrate glycans on the heavy chains of the deglycosylated DFO-hSC16 and DFO-hSC16 Fc-silent immunoconjugates.

ImmunoPET imaging with ^{89}Zr-labeled deglycosylated-DFO-hSC16 yielded high PET signal in the H82 tumor and remarkably low background in NSG mice (Fig. 2D). *Ex vivo* biodistribution analysis yielded fair agreement with the PET images, demonstrating a restoration of the radioactivity concentration (25.4% ± 10.9% ID/g in H82 tumors, which was comparable with the concentrations observed in H82 tumors of Nu/Nu mice xenografts (Fig. 2E; Supplementary Table S2). A 4- to 6-fold drop in the activity concentration was observed in the spleen along with approximately 2-fold decreased activity concentration in the liver and bones of NSG mice xenografts injected with ^{89}Zr-labeled deglycosylated-DFO-hSC16. A similar biodistribution pattern was obtained for the Fc-silent hSC16 radioimmunoconjugate. The *in vivo* biodistribution of the Fc-silent hSC16 radiotracer was agnostic to the immunodeficient background of the mouse strain (Nu/Nu vs. NSG) or the presence of an excess of the isotype-matched humanized antibody (Fig. 2D–E; Supplementary Table S3).

Applicability to other tumor models and therapeutic mAbs

This anomalous pattern of *in vivo* biodistribution in highly immunodeficient mice extended to other humanized IgG1 antibodies including huJ591 (Fig. 3A) and trastuzumab (Fig. 3B). *Ex vivo* biodistribution analyses of the radioimmunoconjugates synthesized from both these humanized antibodies displayed higher activity concentrations in the spleen, bones, and liver compared with the tumors in highly immunodeficient mice (Fig. 3C and D; Supplementary Tables S4

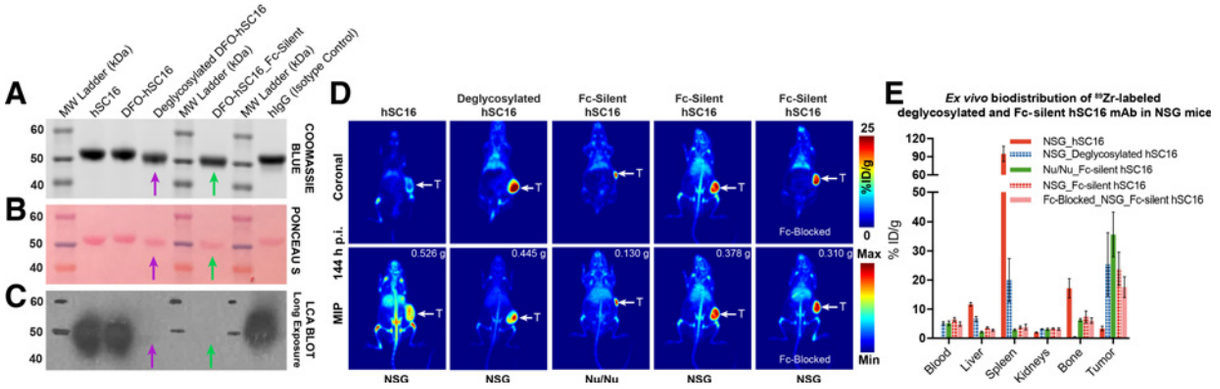

Figure 2.

Deglycosylated and Fc-silent variants of humanized antibodies can escape Fc-mediated uptake in nontarget organs of highly immunodeficient mice. **A,** Gel electrophoresis of various hSC16 constructs showing a downward shift in the mobility of antibody heavy chains from the chemoenzymatically deglycosylated DFO-hSC16 (purple arrow) and the DFO-conjugated Fc-silent variant of hSC16 (green arrow). **B,** Ponceau S–stained nitrocellulose membrane showing successful transfer of protein from the gel. **C,** Lens culinaris agglutinin (LCA) blot showing absence of glycans on the heavy chains of the Fc-engineered hSC16 antibody immunoconjugates. **D** and **E,** PET images and *ex vivo* biodistribution analysis of ^{89}Zr-labeled deglycosylated and Fc-silent hSC16 radioimmunoconjugates in Nu/Nu versus NSG mice bearing H82 tumors showing highly specific uptake of the radiotracer in the tumors in both strains. The tumor weights are given at the top right-hand corner of the MIP images. %ID/g values are shown in Supplementary Tables S2 and S3.

and S5). SKOV3 tumors were strongly delineated in PET images of Nu/Nu as well as NSG mice xenografts; however, marginally better tumor-to-background contrast was obtained in Nu/Nu mice (Fig. 3B). Notably, although the uptake of ^{89}Zr-labeled trastuzumab in the spleen of NSG mice was relatively high, it could be blocked by coinjection of a 25-fold excess of the unlabeled isotype-matched humanized antibody. By doing so, the activity concentrations in nontarget organs such as the spleen, bones, and liver could be effectively normalized and the tumoral uptake of the Her2-targeted radiotracer could be restored (Fig. 3D).

Impact of the role of chimerization and biological origin of mAbs on their *in vivo* pharmacologic profile in highly immunodeficient mice

Finally, to investigate the effect of inter-species Fc-FcR interaction on the *in vivo* biodistribution of chimeric versus murine antibodies, ^{89}Zr-labeled radioimmunoconjugates were prepared using cetuximab, a chimeric antibody that is clinically used for targeting EGFR-overexpressing tumors, and mSC16, a murine mAb precursor of the humanized DLL3-targeted antibody. The *in vivo* profile of cetuximab resembled the anomalous biodistribution pattern observed for humanized IgG1 antibodies. Briefly, low tumor uptake and high Fc-mediated nontarget accumulation of activity concentrations of ^{89}Zr-labeled cetuximab was observed in the PET images of NSG mice xenografts (Fig. 4A). On the other hand, mSC16 yielded high contrast and qualitatively comparable PET images of H82 tumors in Nu/Nu as well as NSG mice xenografts. The liver was delineated in the background of PET images from H82 xenografts in both strains (Fig. 4B). Similar to the humanized antibodies analyzed in this study, the anomalous biodistribution pattern of cetuximab could be reversed by coinjection of a 25-fold excess of the isotype-matched humanized antibody (Fig. 4C; Supplementary Table S6). On the other hand, biodistribution studies of ^{89}Zr-labeled mSC16 yielded a comparable uptake of the tracer in H82 tumors and the livers of xenograft mice from both strains. Despite a relatively higher concentration of activity in the spleen and bones of NSG mice, the uptake of the murine variant of the DLL3-targeting antibody in the tumor remained unaffected by the coinjection of an excess of the unlabeled anti-hapten humanized antibody (Fig. 4D; Supplementary Table S7).

Low endogenous immunoglobulin titers lead to the anomalous biodistribution of humanized antibodies in NSG mice

On the basis of the recurring theme of high splenic concentration of activity (per unit mass of tissue) for humanized antibody tracers injected in NSG mice, we hypothesized that this tissue might be the driver for the altered *in vivo* antibody pharmacokinetics. We sought to interrogate its role and contribution to the anomalous biodistribution patterns that were observed. Contrary to our expectations, PET imaging and biodistribution studies showed no rerouting of ^{89}Zr-labeled hSC16 to the tumor in splenectomized mice, thus ruling out the spleen as the major nontarget sink in NSG mice (Fig. 5A and B; Supplementary Table S8).

Next, we investigated whether the lack of endogenous immunoglobulin due to the absence of B cells in highly immunodeficient mice might be causing the anomalous biodistribution pattern observed in these strains. SCID mice showed extremely low titer (<5 μg/mL) of IgM, whereas NOD SCID and NSG mice showed near complete absence of titers for all immunoglobulins tested (Figure S3). This result combined with the ability of the co-injected 25-fold excess of isotype-matched anti-hapten humanized antibody to consistently reverse the anomalous biodistribution pattern pointed to a plausible role played by the lack of FcR occupancy due to endogenous immunoglobulins being absent in highly immunodeficient mice. To test this hypothesis, we exogenously reconstituted the immunoglobulin titers in H82 xenograft NSG mice with IgG isolated from mouse serum. Mice injected with 1 mg of mouse IgG an hour prior to the injection of ^{89}Zr-labeled hSC16 showed normal biodistribution patterns in nontarget organs and high tumor uptake of the DLL3-targeted antibody tracer at 144 hours, whereas mice ($N = 5$) that were not preinjected with

the mouse IgG displayed the anomalous biodistribution patterns that were previously observed in NSG mice (Fig. 5C; Supplementary Table S9).

Furthermore, since the severely hypoplastic spleens in highly immunodeficient strains may artificially accentuate the degree of activity calculated in the %ID/g readout, we performed a secondary analysis for biodistribution using the non-normalized % ID readout. This unequivocally demonstrated that the liver and the bones were among the major nontarget organ sinks for humanized IgG1 antibodies in NSG mice (Fig. 5D; Supplementary

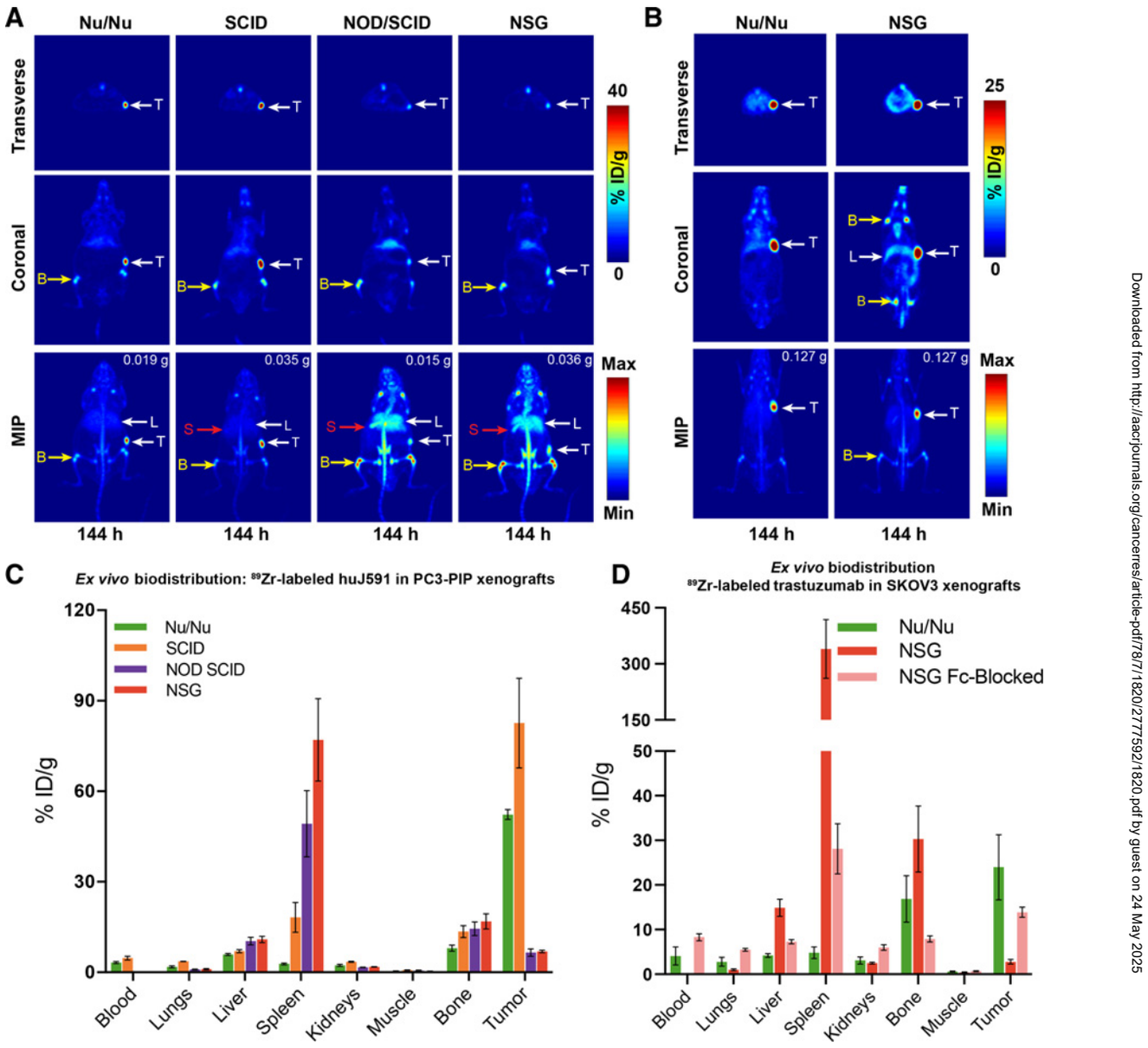

Figure 3.

A recurring theme of Fc-mediated reversible off-target *in vivo* biodistribution of humanized therapeutic antibodies in highly immunodeficient mice. **A,** PET images acquired at 142–146 hours after the injection of ^{89}Zr-labeled huJ591 in PSMA-positive PC3-PIP xenografts developed in a spectrum of immunodeficient background (increasing from left to right): Nu/Nu < SCID << NOD SCID <<< NSG. PET images showing the delineation of similarly sized subcutaneous PC3-PIP tumors with different activity concentration and signal intensities in the various strains. MIP images of the highly immunodeficient NOD SCID and NSG mice show higher signal and activity concentrations in the spleen (S), bone (B), and liver (L). **B,** PET images acquired at 148–150 hours after the injection of ^{89}Zr-labeled trastuzumab in Her2-positive SKOV3 xenografts in Nu/Nu mice (left) versus NSG mice (right). PET images reveal strongly delineated PET-avid SKOV3 tumors in both strains; however, NSG mice showed relatively higher background signal in the bone (B) and liver (L). **C,** *Ex vivo* biodistribution analysis of ^{89}Zr-labeled huJ591 antibody at 144 hours after the injection of the tracer, showing activity concentrations in PC3-PIP tumors and selected nontarget organs from xenograft mice with varying immunodeficient backgrounds. **D,** *Ex vivo* biodistribution of ^{89}Zr-labeled trastuzumab at 144 hours after the injection of the tracer, showing the concentration of radioactivity in SKOV3 tumors and select nontarget organs from Nu/Nu versus NSG xenograft mice. The tumor weights are given at the top right-hand corner of the MIP images. %ID/g values are shown in Supplementary Tables S4 and S5.

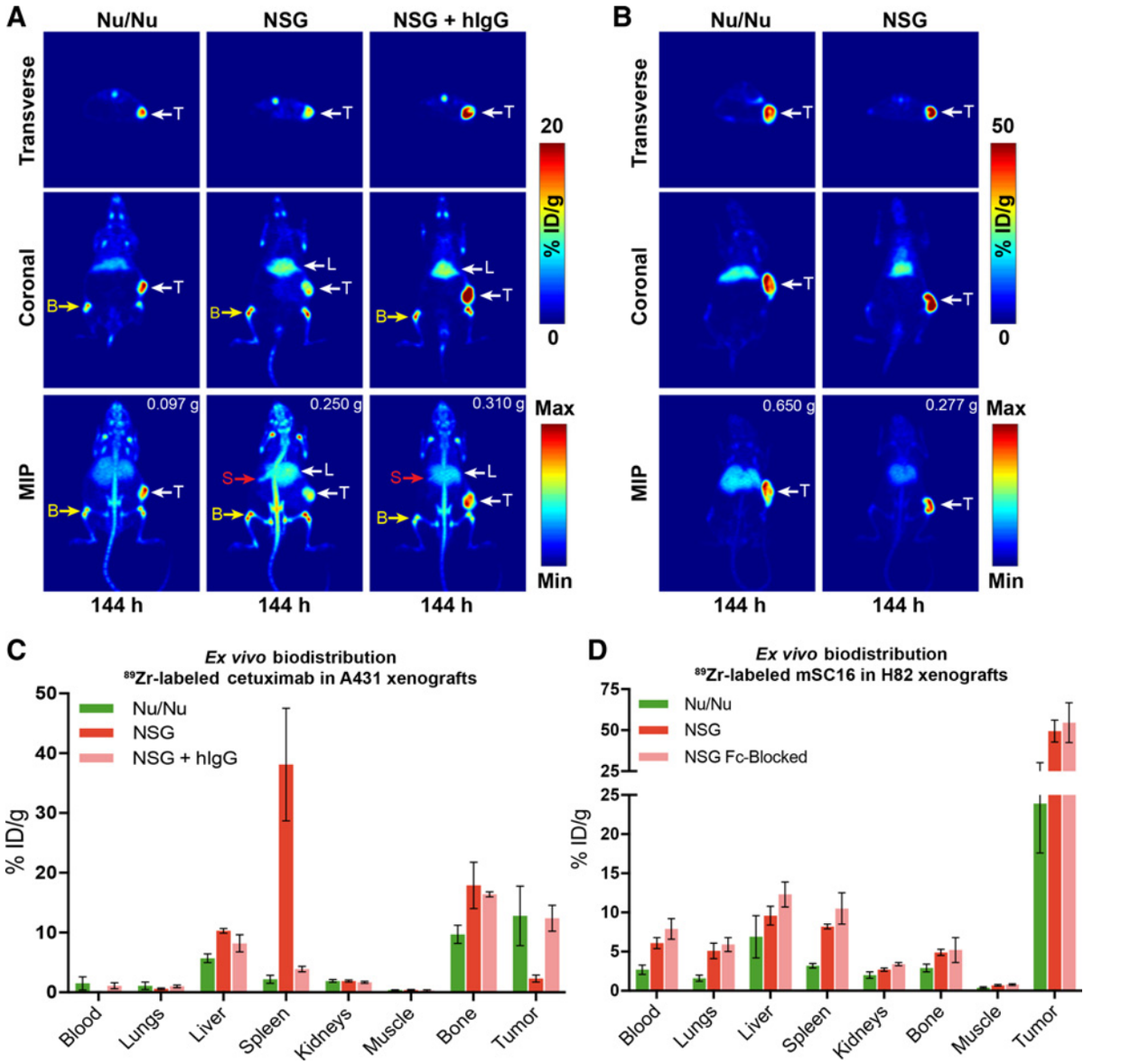

Figure 4.

Chimeric antibodies are subject to Fc-mediated anomalous *in vivo* biodistribution in NSG mice, but murine antibodies are indifferent to the immunodeficiency status of the preclinical host. **A,** PET images of ^{89}Zr-labeled cetuximab in EGFR-positive A431 xenografts in Nu/Nu versus NSG mice showing relatively higher specific uptake of the radiotracer in the tumors of Nu/Nu mice. **B,** PET images of ^{89}Zr-labeled mSC16 antibody acquired at 144–146 hours after the injection of the tracer in H82 xenografts in Nu/Nu (left) versus NSG mice (right). PET images revealed well-delineated H82 tumors with high uptake, while also highlighting the liver (L) in the background of mice from both strains. **C,** *Ex vivo* biodistribution analysis of ^{89}Zr-labeled cetuximab revealing the anomalous pattern for high splenic concentration of activity and concomitantly low uptake in the tumors of NSG mice xenografts. A reversal of this pattern and decreased nontarget organ accumulation was obtained by coinjection of a 50-fold excess of the humanized isotype control antibody in NSG mice xenografts. %ID/g values are shown in Supplementary Table S6. **D,** *Ex vivo* biodistribution of ^{89}Zr-labeled mSC16 antibody at 144 hours postinjection showed no differences in the biodistribution of the tracer between Nu/Nu versus NSG xenograft mice. A slightly higher concentration of activity was found in the blood, spleen, and bones of NSG mice. However, coinjection of a 42- to 50-fold excess of humanized anti-hapten antibody did not significantly alter the *in vivo* radiopharmacologic profile of the murine antibody-based tracer in NSG mice. The tumor weights are given at the top right-hand corner of the MIP images. %ID/g values are shown in Supplementary Table S7.

Table S10). This was further supported by *ex vivo* biodistribution performed at early time points revealing a rapid accretion of ^{89}Zr-labeled hSC16 in the liver and bones of tumor-bearing NSG mice within the first 24 hours after injection of the tracer (Fig. 5E; Supplementary Table S11).

Histopathologic analysis of treated animals

Notably, NSG mice xenografts injected with imaging doses [7.4–9.25 MBq; (200–250 μCi), 35–44 μg] of ^{89}Zr-labeled humanized antibodies, hSC16, huJ591, trastuzumab, and the chimeric antibody cetuximab, were moribund with occasional

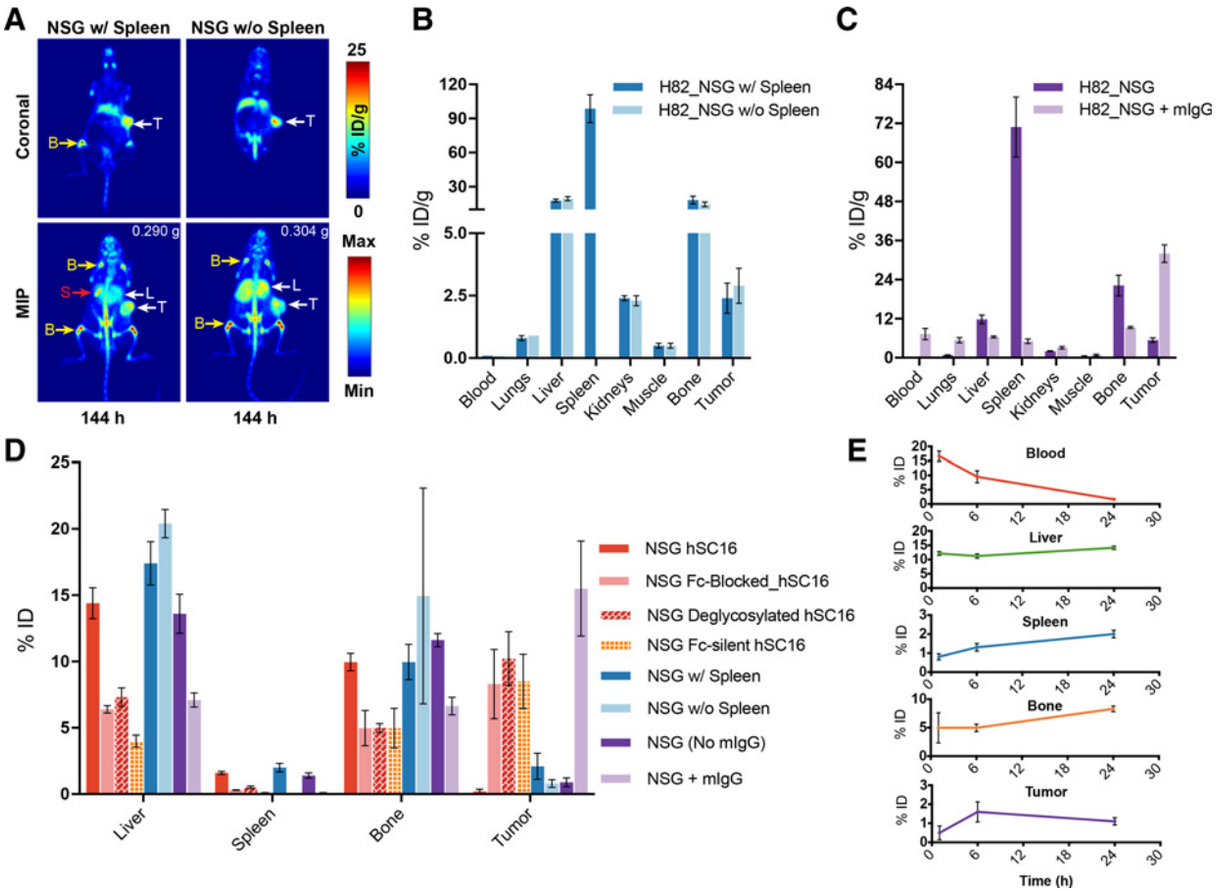

Figure 5.

Absence of endogenous IgG leads to the anomalous biodistribution of humanized antibodies in NSG mice. PET images (**A**) and *ex vivo* biodistribution analysis (**B**) of NSG H82 xenograft mice with (w/) and without (w/o) spleen, showing no significant difference in the *in vivo* radiopharmacologic profile of the ^{89}Zr-labeled hSC16 antibody. The tumor weights are given at the top right-hand corner of the MIP images. %ID/g values are shown in Supplementary Table S8. **C,** *Ex vivo* biodistribution of ^{89}Zr-labeled hSC16 antibody in NSG H82 xenograft mice versus those preinjected with 1 mg of murine IgG showing a reversal of the anomalous biodistribution by reconstituting the antibody titers in NSG mice prior to injection of the ^{89}Zr-labeled hSC16 antibody tracer. %ID/g values are shown in Supplementary Table S9. **D,** A plot showing the percent injected dose (% ID) on the *y*-axis from the various experiments using NSG H82 xenografts and the humanized SC16 antibody tracer to identify the major nontarget tissue sinks bereft of the contribution of the weight (g) of the tissue. %ID values are shown in Supplementary Table S10. **E,** A time course *ex vivo* biodistribution analysis demonstrating the *in vivo* pharmacokinetics of ^{89}Zr-labeled hSC16 and the rapidly increasing accretion of activity (% ID) in the liver, spleen, and bone within the first 24 hours after the injection of the tracer.

cases of death between 11 and 12 days after the injection of the antibody-based tracer. The *ex vivo* histopathologic examination of these animals via gross necropsy and histopathology revealed extensive hemorrhages in multiple tissues and histologic evidence of bacteremia in these animals that would ultimately lead to their death from progressive sepsis. Complete blood count (CBC) examination from these mice at day 12 revealed marked leukopenia and thrombocytopenia and nonregenerative anemia. Furthermore, in comparison with the spleens harvested from experimentally naïve NSG mice or H82 xenografts in NSG mice injected with nonradiolabeled hSC16 antibody, the spleens from mice that were injected with imaging doses of the ^{89}Zr-labeled hSC16 tracer were significantly decreased in size and demonstrated hematopoietic aplasia, which was not prevented by the preinjection of an excess of the humanized isotype control antibody (Fig. 6A). Conversely, the spleens of Nu/Nu mice xenografts injected with the same dose of ^{89}Zr-labeled hSC16 showed no decrease in the size and weight of the spleen or any changes to architecture and cellularity of this tissue harvested from experimentally naïve Nu/Nu mice (Fig. 6B). A similar hematopoietic aplasia was observed in the bone marrows examined from NSG mice xenografts injected with the ^{89}Zr-labeled hSC16 antibody (Fig. 6C and D). The salient and common feature in the spleen and bone marrow was the marked hematopoietic aplasia in these nontarget organs that harbored the highest radioactive concentrations in NSG mice.

To further evaluate the differential Fc-mediated uptake of humanized antibodies between NSG and Nu/Nu mice, we performed *ex vivo* flow cytometry analyses after intravenous administration of a FITC-labeled hSC16 antibody. Consistent with the results of ^{89}Zr-labeled hSC16, NSG mice had a higher FITC fluorescence (measured by mean fluorescent intensity, MFI) in spleen, liver, and bone marrow hematopoietic cells. One

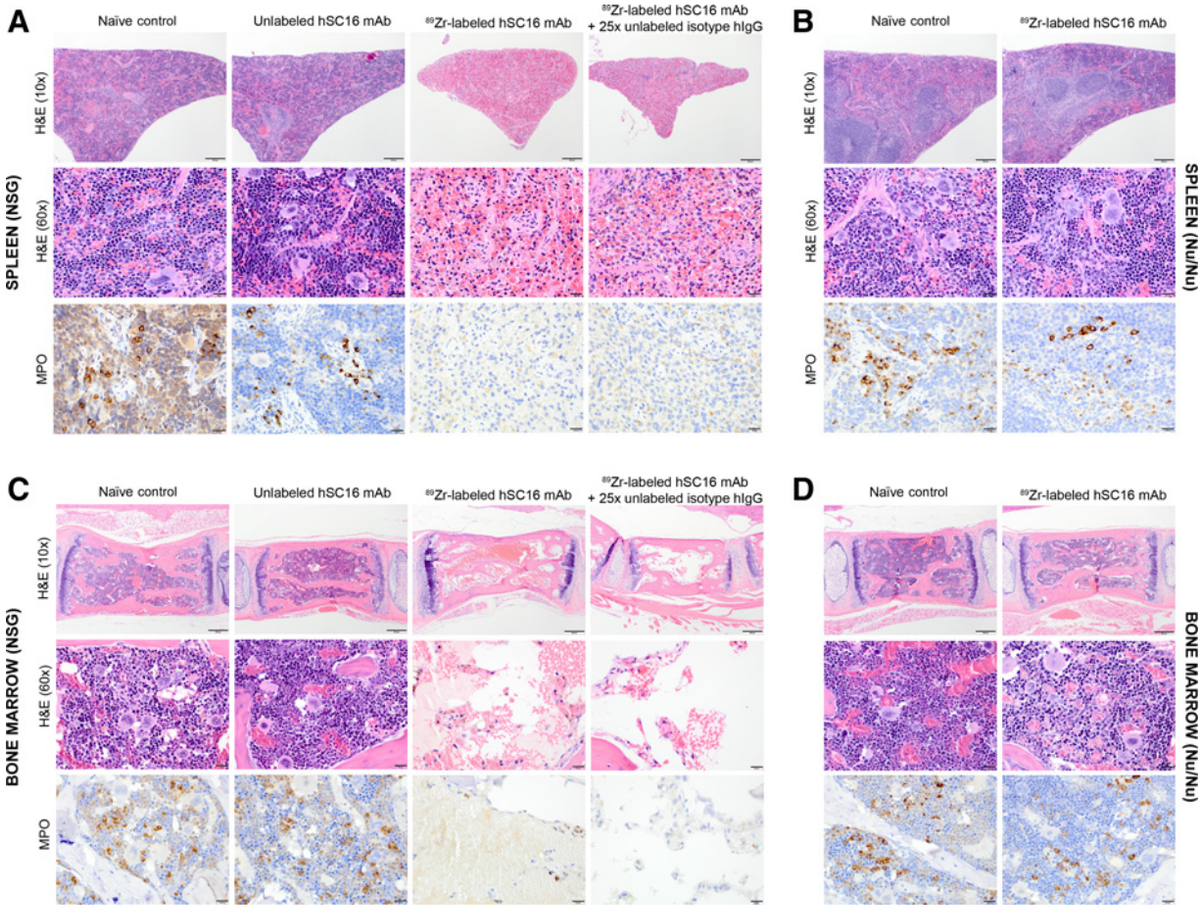

Figure 6.

Fc-mediated anomalous *in vivo* biodistribution of radiolabeled humanized antibodies in highly immunodeficient mice causes hematopoietic aplasia in the spleen and bone marrow. **A,** H&E- and myeloperoxidase (MPO)-stained images of cross sections of the spleens harvested from NSG mice showing normal splenic histology, characterized by absence of white pulp (lymphocytes) and a highly cellular red pulp (hematopoietic cells) in experimentally naïve and NSG H82 xenograft mice injected with unlabeled hSC16. The spleens of NSG H82 xenograft mice injected with the ^{89}Zr-labeled hSC16 show a dramatic loss of cellularity and shrinkage in size regardless of being coinjected with a 25-fold excess of the isotype control antibody used for FcR blockade. **B,** Nude mice spleens showing a characteristic anatomical architecture of white pulp (B-cell follicles) and red pulp (hematopoietic cells) in experimentally naïve mice as well as nude H82 xenografts mice injected with the ^{89}Zr-labeled hSC16. **C,** H&E- and MPO-stained images of cross sections of the femur/sternum harvested from NSG mice showing densely packed marrow with high cellularity in the experimentally naïve mice and those injected with unlabeled hSC16. A marked depletion of cells in this compartment is seen in NSG H82 xenografts injected with the ^{89}Zr-labeled hSC16 regardless of the coinjection with a 25-fold excess of isotype control antibody. **D,** H&E- and MPO-stained images of cross sections of the femur/sternum harvested from nude mice showing densely packed marrow in the experimentally naïve mice and no recognizable loss in cellularity in mice injected with ^{89}Zr-labeled hSC16.

possible explanation is that NSG mice have increased numbers of FcR-expressing myeloid cells. However, with the exception of tissue resident macrophages in the spleen and bone marrow, all other myeloid populations were similar or reduced in number in NSG compared with Nu/Nu mice (Supplementary Fig. S4). Furthermore, NSG mice had largely reduced, rather than increased, expression of FcRI, II/III, and IV compared with Nu/Nu mice (Fig. 7A and B; Supplementary Fig. S5).

We next sought to determine by flow cytometry which organ and cell type represented the largest sink for hSC16. To address this question, we obtained the product of cell number and MFI of each immune cell population in the spleen, liver, and bone marrow. In this analysis, the bone marrow represented the largest sink for hSC16, and this was driven by the fact that the bone marrow compartment had substantially higher cellularity compared with the spleen or liver (Fig. 7C). Neutrophils and monocytes in the bone marrow were identified as the most prominent destinations for hSC16 anomalous binding in the NSG bone marrow (Fig. 7D).

Discussion

The clinical translation of a drug relies heavily on its preclinical performance (13, 26, 27). The ability to transform antibodies into radiotracers and evaluate their tumor-targeting capabilities as well as track their *in vivo* fate via immunoPET imaging and biodistribution studies can be harnessed as a tool to help in the preclinical evaluation of antibody-based drugs. Here, we investigated the impact of two biological parameters with respect to the *in vivo* pharmacology of antibody drugs in a preclinical setting – (i)

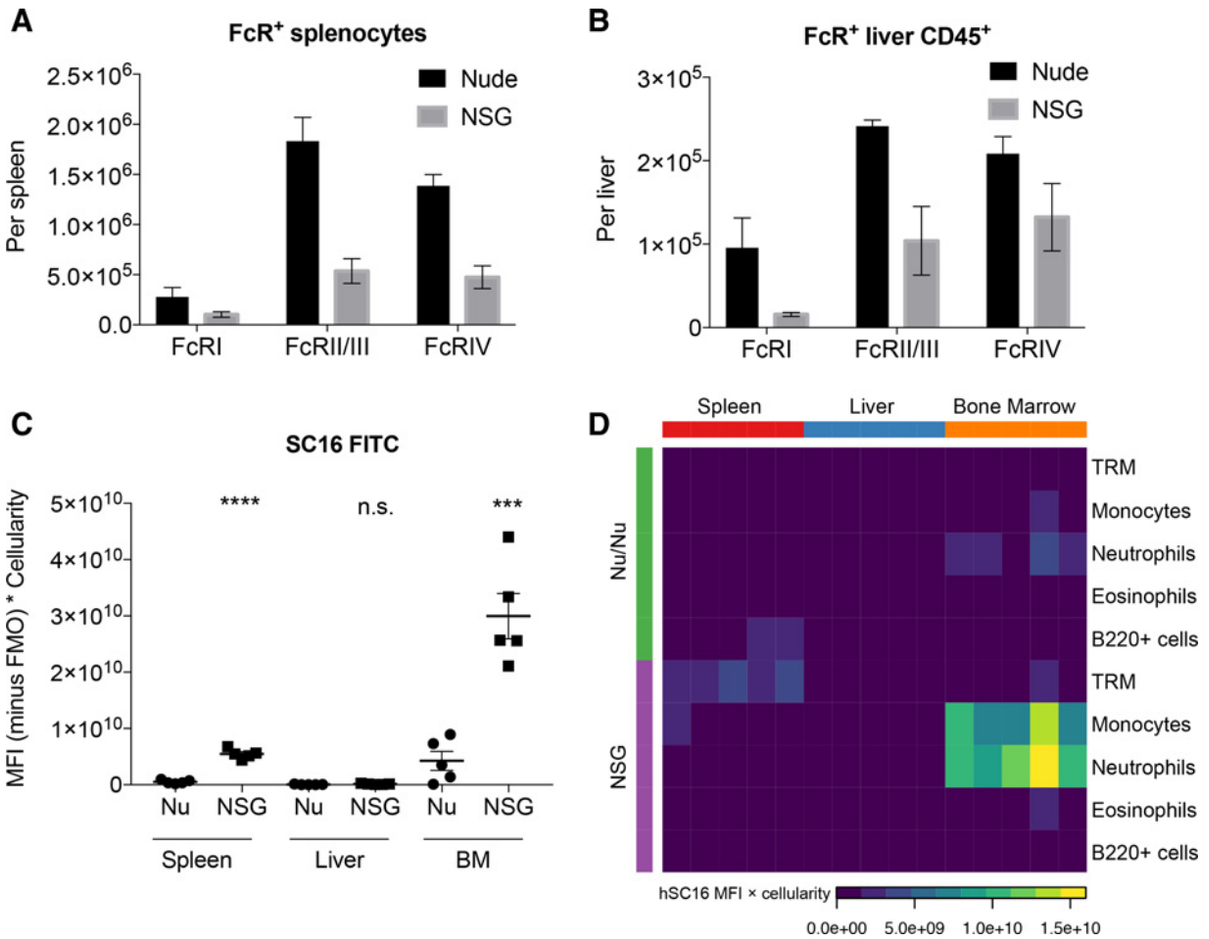

Figure 7.

Ex vivo multicolor flow cytometry characterizes Fc receptor expression in splenic and hepatic myeloid cells and tracks the *in vivo* fate of hSC16. **A** and **B,** FcR expression measured by MFI minus the negative signal in the fluorescence minus one (FMO) control in four immune cell populations of the spleen (**A**) and the liver (**B**) in Nu/Nu and NSG mice ($n = 3$). **C,** Total hSC16 sink in spleen, liver and bone marrow as a product of MFI and tissue cellularity ($n = 5$). Significance testing was performed by Student *t* test (two-sided). ns, nonsignificant, < 0.05; ***, $P \leq 0.001$; ****, $P \leq 0.0001$. **D,** Heatmap of hSC16 localization measured in five immune cell populations from spleen, liver, and bone marrow in Nu/Nu or NSG mice as a product of MFI and tissue cellularity ($n = 5$).

the strain of tumor-bearing animals; and (ii) the biological origin (humanized, chimeric, and murine) and engineered (deglycosylated versus Fc-silent) status of the antibody used to prepare the radiotracers.

In examining the first biological parameter, the choice of a suitable animal model for preclinical research is often driven by multiple factors including the scientific pursuit at hand, the use of established laboratory protocols, time, and economics. A vast majority of preclinical oncologic immunoPET research is carried out in Nu/Nu mice owing to their cost effectiveness and the practical ease of performing subcutaneous and surgical orthotopic engraftment in this strain. However, the noninvasive delineation of sites of distant organ metastases via preclinical immunoPET might warrant the engraftment of clinically relevant tumor lines or cells from patient-derived xenografts (PDX) in mice that are more susceptible to *in vivo* metastasis. Nu/Nu and SCID mice, which have active natural killer (NK) cells, might be limited in their ability to promote metastases (28). However, highly immunodeficient strains such as NSG and NOD SCID mice, which have defective NK cells, reproducibly recapitulate distant organ metastases and provide an ideal environment for the *in vivo* passaging and growth of human PDXs (29).

Despite such advantages offered by NOD SCID and NSG mice, our immunoPET experience in these strains suggests that they might not be well suited for the purpose of preclinical testing of humanized IgG1 antibody-based diagnostic and therapeutic agents, including therapeutic antibody–drug conjugates that may need low-dose administration in preclinical immunodeficient mouse models. We found that the highly immunodeficient background in mice models can *alter* the *in vivo* fate of humanized IgG1 antibody to effectively hijack them to nontarget organs, such as the spleen and bones in these mice, thus dramatically reducing tumor uptake of the antibody-based radiotracer. Notably, the lack of endogenous IgG in mice bearing the *scid* mutation may be one of the factors contributing to the anomalous pattern in the biodistribution of humanized IgG1 in highly immunodeficient mice (30). Our findings lend support to previously demonstrated differences in plasma clearance of antibody–drug conjugates in

NSG versus SCID mice, and plausibly explains the rapid clearance in the NSG strain to be a result of the sequestration of antibody-based agents within the spleen of such highly immunodeficient mice (31). This in itself could dampen the *in vivo* performance of antibody-based radiotracers and the efficacy of therapeutic antibodies by impacting their bioavailability for the intended target expressed by the tumor. More recently, the limited efficacy of antibody–drug conjugates tested in the NSG mouse background has been reported (32).

Nevertheless, we were able to block the exceedingly high concentration of activity in the spleens of NOD SCID and NSG mice xenografts by coinjecting the humanized antibody-based tracer with an excess of the isotype control antibody. Notably, this was a consistently recurring phenomenon documented for a host of humanized antibody candidates that were tested in this study. This points to a role played by the interaction between the Fc-portion of antibody-based drugs and the cells expressing FcRs in nontarget organs. In addition to having myeloid cells such as monocytes and neutrophils, NSG mice are known to have Fc-gamma receptor (FcγR)-expressing innate immune effector cells such as immature macrophages and dendritic cells within the bone marrow, liver, and blood (33, 34). In humans, nonlymphoid organs such as the liver show FcγR expression on resident macrophages known as Kupffer cells (35). Thus, the existing clinical practice of performing immunoPET imaging with ^{89}Zr-labeled antibody tracers after preinjecting patients with an excess amount (mass) of unlabeled antibody plausibly allows for the *in vivo* occupancy of FcR sites in nontarget organs and improves the *in vivo* delineation of tumor lesions to yield better tumor-to-background ratios (22, 36).

Our findings of the inefficient tumor targeting and high off-target binding of humanized antibodies in highly immunodeficient mice are of direct significance to preclinical radioimmunotherapy studies to treat subcutaneously xenografted PDX tumors or distant organ metastases in NSG mice. From an immunoPET perspective, with the exception when immune cells are being imaged, a high concentration of radioactivity in the spleen of Nu/Nu mice xenografts of solid tumors would usually indicate the *in vivo* aggregation of antibody-based radiotracers. However, our results suggest that this may not hold true if the immunoPET strategy is being investigated in xenograft models developed in NSG or NOD SCID mice. Ultimately, if the use of a highly immunodeficient background provided by NOD SCID or NSG mice is indispensable to the preclinical investigation, it might be useful to consider a blockade of the FcR-mediated sequestration of antibody-based radiotracers in nontarget organs.

As an alternative to FcR blockade, our study demonstrates that the contribution of antibody glycosylation to Fc–FcR interaction can be harnessed to evade the sequestration of humanized antibody tracers in nontarget organs of highly immunodeficient mice. It is well known that the binding of an antibody's Fc portion with the various FcRs is glycosylation-dependent (37). Conversely, Fc binding to the neonatal Fc receptor (FcRn) is independent of the glycosylation status of antibodies, but highly pH-dependent (38). The dramatic restoration of tumor uptake for the deglycosylated and Fc-silent variants of the hSC16 antibody radiotracer combined with the significant drop in activity concentrations in nontarget organs of NSG mice to levels that are comparable with those obtained in the FcR blockade experiments for this tracer suggest a convergence on the Fc–FcR axis.

However, the employment of such Fc–FcR blockade strategies might only offer a temporary solution when directly radiolabeled antibodies are used as tracers for radioimmunoimaging or as vectors for the delivery of targeted radiotherapy to tumors *in vivo*. This assertion is based on our documented observation in mice that received imaging doses of ^{89}Zr-labeled hSC16 soon after the preinjection of an excess of the unlabeled isotype control antibody to effectively block FcR sites *in vivo*. While these mice appeared healthy and alert compared with the moribund mice in the unblocked group prior to necropsy on day 12, they had radioactivity in their blood samples, indicative of a persistence of the radiolabeled antibody in systemic circulation over an extended period of time. Histopathologic examination of these mice revealed an equally ablated hematopoietic repertoire in the spleen and bone marrow as seen for mice in the unblocked group (Fig. 6A–D). Such a lack of rescue from FcR blockade in NSG mice xenografts may be attributed to the relatively high radiosensitivity of this strain due to a mutation in the *Prkdc* gene that is implicated in DNA repair (39, 40). Arguably, the highly perfused anatomy of the spleen and bone marrow combined with the acute radiosensitivity of hematopoietic cells therein might be sufficient to ablate them during the transient passage of radiolabeled antibodies through these sites despite FcR blockade in highly immunodeficient mice (41). Notably, NSG xenograft mice that were injected with imaging doses of deglycosylated or Fc-silent ^{89}Zr-labeled hSC16 were ultimately moribund by the end of 3 weeks postinjection of the radiotracer.

Furthermore, the modulation of the *in vivo* biodistribution, pharmacology, and efficacy of antibody-based drugs via Fc–FcR interactions between antibodies and tumor-associated macrophages within the tumor microenvironment has been highlighted by recent reports demonstrating its role in the context of immunotherapies targeting the PD-1/PD-L1 axis as well as tumor-targeted antibody–drug conjugates (42–44). In addition to being directly applicable to antibody-based imaging and radioimmunotherapy, our results may be of value to allied areas of preclinical research including those that utilize highly immunodeficient mice for testing the efficacy of therapeutic antibodies and antibody-based agents such as ADCs and Fc-fusion molecules for oncologic drug development, and immune disorders. Taken together, our findings demonstrate the critical role played by the lack of endogenous immunoglobulins that can lead to the anomalous *in vivo* biodistribution patterns and altered pharmacokinetics of humanized antibodies. Our findings also provide alternative solutions to reverse the altered pharmacokinetics of antibody-based drugs in highly immunodeficient preclinical mouse models via FcR occupancy or FcR evasion strategies.

Finally, our experiments highlight a substantially different *in vivo* navigation by murine IgG1 antibodies versus their humanized counterparts in the highly immunodeficient background of NSG mice. Our findings suggest that the *in vivo* biodistribution and immunoPET performance of equivalent doses of ^{89}Zr-labeled antibody tracers derived from murine IgG1 remain unaffected by the difference in the immunodeficiency status of the mouse strain, or by the coinjection of an excess of the nonspecific humanized antibody used for FcR blockade. In part, this might be due to a preferential interaction or a difference in the binding affinity of the Fc portions of murine versus humanized IgG1 antibodies for FcR-expressing immune cells. Furthermore, humanized therapeutic antibodies are usually designed to have Fc regions that can induce antibody-dependent cell-mediated

cytotoxicity (ADCC) via engagement of activating FcRs on immune effector cells *in vivo*. Trastuzumab is an example of one such humanized therapeutic antibody (45–47). This aspect might plausibly explain the significantly higher splenic uptake of ^{89}Zr-labeled trastuzumab in NSG mice compared with the hSC16 antibody, which is rapidly internalized upon binding to its target (DLL3) and was not explicitly developed for ADCC activity. On the other hand, the lower uptake of ^{89}Zr-labeled mSC16 versus ^{89}Zr-labeled hSC16 in the spleen and bones of NSG mice might be explained by the broad-spectrum interaction of humanized IgG1 antibodies with three activating mouse FcRs, whereas murine IgG1 antibodies interact with only one activating mouse FcR. In addition, murine IgG1 antibodies have a relatively higher affinity than humanized variants for the inhibitory mouse Fc-receptor FcγRIIb (48–50).

Conclusion

In summary, our study suggests that much of the anomalous biodistribution of humanized antibody drugs in highly immunodeficient mice may be attributed to an avid Fc-mediated binding of these agents to FcR-expressing myeloid cells in nontarget organs when endogenous immunoglobulin levels are low or nearly absent. The work at hand has important implications for the evaluation of Fc-containing therapeutics in immunodeficient mice models and highlights a clear need for biodistribution studies to be performed in the early stages of an antibody-based drug development campaign.

Disclosure of Potential Conflicts of Interest

No potential conflicts of interest were disclosed.

Authors' Contributions

Conception and design: S.K. Sharma, S. Monette, B.M. Zeglis, J.T. Poirier, J.S. Lewis

Development of methodology: S.K. Sharma, S. Monette, B.M. Zeglis, J.T. Poirier, J.S. Lewis

Acquisition of data (provided animals, acquired and managed patients, provided facilities, etc.): S.K. Sharma, A. Chow, S. Monette, D. Vivier, J. Pourat, D. Abdel-Atti, J.S. Lewis

Analysis and interpretation of data (e.g., statistical analysis, biostatistics, computational analysis): S.K. Sharma, A. Chow, S. Monette, J.T. Poirier, J.S. Lewis

Writing, review, and/or revision of the manuscript: S.K. Sharma, A. Chow, S. Monette, B.M. Zeglis, J.T. Poirier, J.S. Lewis

Administrative, technical, or material support (i.e., reporting or organizing data, constructing databases): S.K. Sharma, K.J. Edwards, T.R. Dilling, D. Abdel-Atti, J.S. Lewis

Study supervision: S.K. Sharma, B.M. Zeglis, J.T. Poirier, J.S. Lewis

Acknowledgments

The authors gratefully acknowledge the MSKCC Small-Animal Imaging Core Facility, the Radiochemistry and Molecular Imaging Probe Core, and the Laboratory of Comparative Pathology, which were supported in part by NIH grant P30 CA08748. The work was also supported by a grant from the Druckenmiller Center for Lung Cancer Research (to J.T. Poirier, J.S. Lewis) and NIH grants U01 CA213359 (to J.T. Poirier) and R01 CA213448 (to J.T. Poirier, J.S. Lewis). We would also like to acknowledge funding from NIH T32 CA009512-29A1 (to A. Chow). The authors also thank Mr. William H. and Mrs. Alice Goodwin and the Commonwealth Foundation for Cancer Research and the MSK Center for Experimental Therapeutics.

The costs of publication of this article were defrayed in part by the payment of page charges. This article must therefore be hereby marked *advertisement* in accordance with 18 U.S.C. Section 1734 solely to indicate this fact.

Received June 30, 2017; revised November 23, 2017; accepted January 19, 2018; published OnlineFirst January 23, 2018.

References

1. Reichert JM. Antibodies to watch in 2017. MAbs 2017;9:167–81.
2. Geng X, Kong X, Hu H, Chen J, Yang F, Liang H, et al. Research and development of therapeutic mAbs: An analysis based on pipeline projects. Hum Vaccin Immunother 2015;11:2769–76.
3. Ecker DM, Jones SD, Levine HL. The therapeutic monoclonal antibody market. MAbs 2015;7:9–14.
4. Hay M, Thomas DW, Craighead JL, Economides C, Rosenthal J. Clinical development success rates for investigational drugs. Nat Biotechnol 2014;32:40–51.
5. Kohler G, Milstein C. Continuous cultures of fused cells secreting antibody of predefined specificity. Nature 1975;256:495–7.
6. Yelton DE, Scharff MD. Monoclonal antibodies: a powerful new tool in biology and medicine. Annu Rev Biochem 1981;50:657–80.
7. Jakobovits A, Amado RG, Yang X, Roskos L, Schwab G. From XenoMouse technology to panitumumab, the first fully human antibody product from transgenic mice. Nat Biotechnol 2007;25:1134–43.
8. Murphy AJ, Macdonald LE, Stevens S, Karow M, Dore AT, Pobursky K, et al. Mice with megabase humanization of their immunoglobulin genes generate antibodies as efficiently as normal mice. Proc Natl Acad Sci U S A 2014;111:5153–8.
9. Cervenak J, Kurrle R, Kacskovics I. Accelerating antibody discovery using transgenic animals overexpressing the neonatal Fc receptor as a result of augmented humoral immunity. Immunol Rev 2015;268:269–87.
10. Day CP, Merlino G, Van Dyke T. Preclinical mouse cancer models: a maze of opportunities and challenges. Cell 2015;163:39–53.
11. Ernst W. Humanized mice in infectious diseases. Comp Immunol Microbiol Infect Dis 2016;49:29–38.
12. Clohessy JG, Pandolfi PP. Mouse hospital and co-clinical trial project–from bench to bedside. Nat Rev Clin Oncol 2015;12:491–8.
13. Gould SE, Junttila MR, de Sauvage FJ. Translational value of mouse models in oncology drug development. Nat Med 2015;21:431–9.
14. Rodgers KR, Chou RC. Therapeutic monoclonal antibodies and derivatives: Historical perspectives and future directions. Biotechnol Adv 2016;34:1149–58.
15. Matthews PM, Rabiner I, Gunn R. Non-invasive imaging in experimental medicine for drug development. Curr Opin Pharmacol 2011;11:501–7.
16. de Vries EG, Oude Munnink TH, van Vugt MA, Nagengast WB. Toward molecular imaging-driven drug development in oncology. Cancer Discov 2011;1:25–8.
17. O'Connor JP, Aboagye EO, Adams JE, Aerts HJ, Barrington SF, Beer AJ, et al. Imaging biomarker roadmap for cancer studies. Nat Rev Clin Oncol 2017;14:169–86.
18. Mankoff DA, Farwell MD, Clark AS, Pryma DA. How imaging can impact clinical trial design: molecular imaging as a biomarker for targeted cancer therapy. Cancer J 2015;21:218–24.
19. Kraeber-Bodere F, Bailly C, Cherel M, Chatal JF. ImmunoPET to help stratify patients for targeted therapies and to improve drug development. Eur J Nucl Med Mol Imaging 2016;43:2166–8.
20. Bailly C, Clery PF, Faivre-Chauvet A, Bourgeois M, Guerard F, Haddad F, et al. Immuno-PET for clinical theranostic approaches. Int J Mol Sci 2016;18. doi: 10.3390/ijms18010057.
21. Wright BD, Lapi SE. Designing the magic bullet? The advancement of immuno-PET into clinical use. J Nucl Med 2013;54:1171–4.
22. Jauw YW, Menke-van der Houven van Oordt CW, Hoekstra OS, Hendrikse NH, Vugts DJ, Zijlstra JM, et al. Immuno-positron emission tomography with zirconium-89-labeled monoclonal antibodies in oncology: what can we learn from initial clinical trials? Front Pharmacol 2016;7:131.

23. Saunders LR, Bankovich AJ, Anderson WC, Aujay MA, Bheddah S, Black K, et al. A DLL3-targeted antibody-drug conjugate eradicates high-grade pulmonary neuroendocrine tumor-initiating cells in vivo. Sci Transl Med 2015;7:302ra136.
24. Sharma SK, Pourat J, Abdel-Atti D, Carlin SD, Piersigilli A, Bankovich AJ, et al. Non-invasive interrogation of DLL3 expression in metastatic small cell lung cancer. Cancer Res 2017;77:3931–41.
25. Arnold JN, Wormald MR, Sim RB, Rudd PM, Dwek RA. The impact of glycosylation on the biological function and structure of human immunoglobulins. Annu Rev Immunol 2007;25:21–50.
26. McGonigle P, Ruggeri B. Animal models of human disease: challenges in enabling translation. Biochem Pharmacol 2014;87:162–71.
27. Perrin S. Preclinical research: Make mouse studies work. Nature 2014;507: 423–5.
28. Malladi S, Macalinao DG, Jin X, He L, Basnet H, Zou Y, et al. Metastatic Latency and Immune Evasion through Autocrine Inhibition of WNT. Cell 2016;165:45–60.
29. Shultz LD, Goodwin N, Ishikawa F, Hosur V, Lyons BL, Greiner DL. Human cancer growth and therapy in immunodeficient mouse models. Cold Spring Harb Protoc 2014;2014:694–708.
30. Bosma MJ, Carroll AM. The SCID mouse mutant: definition, characterization, and potential uses. Annu Rev Immunol 1991;9:323–50.
31. Lyon RP, Setter JR, Bovee TD, Doronina SO, Hunter JH, Anderson ME, et al. Self-hydrolyzing maleimides improve the stability and pharmacological properties of antibody-drug conjugates. Nat Biotechnol 2014;32:1059–62.
32. Stefan N, Gebleux R, Waldmeier L, Hell T, Escher M, Wolter FI, et al. Highly potent, anthracycline-based antibody-drug conjugates generated by enzymatic, site-specific conjugation. Mol Cancer Ther 2017;16:879–92.
33. Jonnalagadda M, Mardiros A, Urak R, Wang X, Hoffman LJ, Bernanke A, et al. Chimeric antigen receptors with mutated IgG4 Fc spacer avoid fc receptor binding and improve T cell persistence and antitumor efficacy. Mol Ther 2015;23:757–68.
34. Guilliams M, Bruhns P, Saeys Y, Hammad H, Lambrecht BN. The function of Fcgamma receptors in dendritic cells and macrophages. Nat Rev Immunol 2014;14:94–108.
35. Tuijnman WB, Van Wichen DF, Schuurman HJ. Tissue distribution of human IgG Fc receptors CD16, CD32 and CD64: an immunohistochemical study. APMIS 1993;101:319–29.
36. Dijkers EC, Oude Munnink TH, Kosterink JG, Brouwers AH, Jager PL, de Jong JR, et al. Biodistribution of 89Zr-trastuzumab and PET imaging of HER2-positive lesions in patients with metastatic breast cancer. Clin Pharmacol Ther 2010;87:586–92.
37. Pincetic A, Bournazos S, DiLillo DJ, Maamary J, Wang TT, Dahan R, et al. Type I and type II Fc receptors regulate innate and adaptive immunity. Nat Immunol 2014;15:707–16.
38. Sockolosky JT, Szoka FC. The neonatal Fc receptor, FcRn, as a target for drug delivery and therapy. Adv Drug Deliv Rev 2015;91: 109–24.
39. Pearson T, Shultz LD, Miller D, King M, Laning J, Fodor W, et al. Non-obese diabetic-recombination activating gene-1 (NOD-Rag1 null) interleukin (IL)-2 receptor common gamma chain (IL2r gamma null) null mice: a radioresistant model for human lymphohaematopoietic engraftment. Clin Exp Immunol 2008;154:270–84.
40. Shultz LD, Lyons BL, Burzenski LM, Gott B, Chen X, Chaleff S, et al. Human lymphoid and myeloid cell development in NOD/LtSz-scid IL2R gamma null mice engrafted with mobilized human hemopoietic stem cells. J Immunol 2005;174:6477–89.
41. Cataldi M, Vigliotti C, Mosca T, Cammarota M, Capone D. Emerging role of the spleen in the pharmacokinetics of monoclonal antibodies, nanoparticles and exosomes. Int J Mol Sci 2017;18. doi: 10.3390/ijms18061249.
42. Arlauckas SP, Garris CS, Kohler RH, Kitaoka M, Cuccarese MF, Yang KS, et al. *In vivo* imaging reveals a tumor-associated macrophage-mediated resistance pathway in anti-PD-1 therapy. Sci Transl Med 2017;9. doi: 10.1126/scitranslmed.aal3604.
43. Dahan R, Sega E, Engelhardt J, Selby M, Korman AJ, Ravetch JV. FcgammaRs modulate the anti-tumor activity of antibodies targeting the PD-1/PD-L1 axis. Cancer Cell 2015;28:285–95.
44. Li F, Ulrich M, Jonas M, Stone IJ, Linares G, Zhang X, et al. Tumor associated macrophages can contribute to antitumor activity through FcgammaRmediated processing of antibody-drug conjugates. Mol Cancer Ther 2017;16:1347–54.
45. Petricevic B, Laengle J, Singer J, Sachet M, Fazekas J, Steger G, et al. Trastuzumab mediates antibody-dependent cell-mediated cytotoxicity and phagocytosis to the same extent in both adjuvant and metastatic HER2/neu breast cancer patients. J Transl Med 2013;11:307.
46. Scott AM, Wolchok JD, Old LJ. Antibody therapy of cancer. Nat Rev Cancer 2012;12:278–87.
47. Mellor JD, Brown MP, Irving HR, Zalcberg JR, Dobrovic A. A critical review of the role of Fc gamma receptor polymorphisms in the response to monoclonal antibodies in cancer. J Hematol Oncol 2013;6:1.
48. Overdijk MB, Verploegen S, Ortiz Buijsse A, Vink T, Leusen JH, Bleeker WK, et al. Crosstalk between human IgG isotypes and murine effector cells. J Immunol 2012;189:3430–8.
49. Dekkers G, Bentlage AEH, Stegmann TC, Howie HL, Lissenberg-Thunnissen S, Zimring J, et al. Affinity of human IgG subclasses to mouse Fc gamma receptors. MAbs 2017;9:767–73.
50. Nimmerjahn F, Ravetch JV. Fcgamma receptors as regulators of immune responses. Nat Rev Immunol 2008;8:34–47.